International Journal of Thermophysics

Absorptivity control over the visible to mid-infrared range using a multilayered film consisting of thermochromic vanadium dioxide

--Manuscript Draft--

Manuscript Number:	IJOT-D-21-00644R1
Full Title:	Absorptivity control over the visible to mid-infrared range using a multilayered film consisting of thermochromic vanadium dioxide
Article Type:	Original Research
Keywords:	Thermal radiation; finite difference time domain method; vanadium dioxide; surface plasmon; surface phonon; optical interference
Corresponding Author:	Kazuma Isobe, Ph. D Okayama University: Okayama Daigaku JAPAN
Corresponding Author Secondary Information:	
Corresponding Author's Institution:	Okayama University: Okayama Daigaku
Corresponding Author's Secondary Institution:	
First Author:	Kazuma Isobe, Ph. D
First Author Secondary Information:	
Order of Authors:	Kazuma Isobe, Ph. D
	Minoru Tomioka
	Yutaka Yamada, Ph.D.
	Akihiko Horibe, Ph.D.
Order of Authors Secondary Information:	
Funding Information:	Japan Society for the Promotion of Science (20K22394) — Dr. Kazuma Isobe
Abstract:	Vanadium dioxide (VO 2) is a phase-transition material that exhibits metallic or insulating characteristics depending upon its temperature. In this study, a multilayered film consisting of VO 2 , silicon dioxide (SiO 2) and gold was proposed as a metamaterial that switches its absorptivity over a broad wavelength range depending on the ambient temperature as a fundamental element of a building pigment. At high temperatures, the multilayer showed a high absorptivity at mid-infrared wavelengths, promoting radiative cooling. Simultaneously, the multilayer presented a low absorptivity in the visible and near-infrared wavelengths, enhancing sunlight absorption. The daily average heat flux can possibly be suppressed in summer in comparison with a gray body whose emissivity was 0.8. Conversely, at a lower temperatures, the multilayer showed opposite absorptivity in both the mid-infrared and visible ranges, and its daily average heat flux increased in winter. The metal–insulator phase transition of VO 2 caused a drastic shift of the resonant wavelength related to surface phonons and surface plasmons at an infrared wavelength, and optical interference at a visible wavelength, originating at the interface of the SiO 2 layer. Thus, the radiative heat flux for both sunlight absorption and radiative cooling was simultaneously controlled depending on the temperature of VO 2 .
Response to Reviewers:	First of all, we thank you for your valuable comments and suggestions, which have resulted in modifications that have improved the quality and clarity of our paper. To address each specific point clearly, we have separated the referees' comments into question areas and answered them in turn. Please find attached the answer sheet and revised manuscript with marked changes.

Title

Absorptivity control over the visible to mid-infrared range using a multilayered film consisting of thermochromic vanadium dioxide

Author

Kazuma Isobe[*1], Minoru Tomioka[2], Yutaka Yamada[1], Akihiko Horibe[1]

1. Graduate School of Natural Science and Technology, Department of Mechanical Engineering, Okayama University, Tsushima-naka 3-1-1, Kita-ku, Okayama, 700-8530, Japan

2. Faculty of Engineering, Department of Mechanical Engineering, Okayama University, Tsushima-naka 3-1-1, Kita-ku, Okayama, 700-8530, Japan

[*]Corresponding author

Kazuma Isobe

E-mail: ~~isobe.k.ad@okauama-u.ac.jp~~ isobe.k.ad@okayama-u.ac.jp

Keywords

Thermal radiation, finite difference time domain method, vanadium dioxide, surface plasmon, surface phonon, optical interference

Statements and Declarations

The authors declare that they have no known competing financial interests or personal relationships that could have appeared to influence the work reported in this paper.

Abstract

Vanadium dioxide (VO_2) is a phase-transition material that exhibits metallic or insulating characteristics depending upon its temperature. In this study, a multilayered film consisting of VO_2, silicon dioxide (SiO_2) and gold was proposed as a metamaterial that switches its absorptivity over a broad wavelength range depending on the ambient temperature as a fundamental element of a building pigment. At high temperatures, the multilayer showed a high absorptivity at mid-infrared wavelengths, promoting radiative cooling. Simultaneously, the multilayer presented a low absorptivity in the visible and near-infrared wavelengths, enhancing sunlight absorption. The daily average heat flux can possibly be suppressed in summer in comparison with a gray body whose emissivity was 0.8. Conversely, at a lower temperatures, the multilayer showed opposite absorptivity in both the mid-infrared and visible ranges, and its daily average heat flux increased in winter. The metal–insulator phase transition of VO_2 caused a drastic shift of the resonant wavelength related to surface phonons and surface plasmons at an infrared wavelength, and optical interference at a visible wavelength, originating at the interface of the SiO_2 layer. Thus, the radiative heat flux for both sunlight absorption and radiative cooling was simultaneously controlled depending on the temperature of VO_2.

1. Introduction

The Earth's surface receives solar energy with an intensity of about 1.0 kW/m^2 during the daytime [1]. In contrast, the ground thermally returns radiative energy to outer space depending on its temperature and emissivity through the day and night. The intensities of sunlight and thermal radiation from the ground, i.e., radiative cooling, are not the same from one month to the next. Therefore, we experience seasonal variation with high or low temperatures over the course of each year in most parts of the world. Nowadays, people in developed countries heavily use air-conditioning and heating to maintain comfortable room temperatures, especially in summer and winter. Since these consume much electricity, they can contribute to global warming and the associated climate changes that the world is now experiencing. Moreover, these climate changes promote further consumption of electricity for heating and air-conditioning. To reduce the use of electricity, especially in summer, the use of pigments on building walls and roofs that reflect sunlight have been proposed and commercialized [2–4]. However, their reflective properties prevent sunlight absorption from assisting in heating in winter. To solve this dilemma, researchers have tried to realize intelligent thermochromic windows that have controlled reflectance in response to temperature. In theory, they can reflect sunlight only in summer while absorbing it in the winter [5–8]. Windows have been developed that contain a thermochromic vanadium dioxide (VO_2). They exhibit a reflective property, like a metal, at a high temperature and become transparent, like an insulator, at a lower temperature. Since VO_2 exhibits different crystal structures below

and above its metal–insulator transition temperature, it can have optical, electrical, and thermal properties that significantly change at various temperatures [6,9–11]. To improve the switching property of this material, i.e., the ratio of the optical property before and after phase transition, the growth of VO_2 crystals was done using pulsed laser deposition [12] and chemical vapor deposition [13] as well as sol-gel [6,14,15] and other techniques [9,16]. Several optical metamaterials consisting of VO_2 were studied to improve the switching characteristics of sunlight reflectance at high and low temperatures [12,17–20]. This switching characteristic was also applied to control emissivity at mid-infrared wavelengths to impact radiative cooling of a satellite [19,21]. Moreover, optimized multilayers were proposed to control the absorption and emission of near-infrared rays [22,23]. VO_2 photonic crystals controlling visible ray were promised ways to manufacture synthetic opals [24]. In addition to VO_2, perovskite-type manganese oxide containing rare earth is a candidate material exhibiting metal–insulator transition [11].

Optical metamaterials containing VO_2 as a thermochromic material have attracted the attention of researchers for 20 years. However, each of the earlier investigators independently controlled the optical properties over a limited wavelength range related to sunlight absorption or radiative cooling. Fig. 1 shows spectral radiative intensities of blackbody radiation at 300 K and sunlight considering the transmittance of the atmosphere, i.e., an atmospheric window [1,25]. Sunlight consists visible and near-infrared rays with wavelengths shorter than 2.5 μm, while the ground thermally emits mid-infrared rays at around 10 μm where the atmospheric window transmits the radiation well. Although the net heat flux of radiative cooling is only about 15% of the sunlight

absorption, it cannot be neglected. Since the sun irradiates the ground with a non-uniform intensity throughout the daytime, the daily average solar heat flux is less than half of its maximal value. Therefore, radiative cooling can be promoted even in the daytime by suppressing the absorptivity of visible rays [25–28]. Previous research in both theoretical and experimental approach was often conducted using optical metamaterials that utilized a surface phonon polariton (SPhP) [26] and optical interference [27], while other researchers achieved this effect using no metamaterials [28].

Simultaneous control of sunlight absorption and radiative cooling is necessary to effectively manipulate the heat flux between outer space and the ground. To suppress temperature increases during the summer, the emissivity at the mid-infrared range needs to be high while retaining a low absorptivity in the visible range. In winter, the emissivity, i.e., absorptivity, should have values at the opposite end of the range to increase room temperature. Since it is difficult to achieve such an irregular property with VO_2 alone, we propose a nanometer-sized composite of VO_2 in a metamaterial that has the potential to switch its optical property over a broad wavelength band. In this study, numerical simulations were conducted to clarify the feasibility of developing such an irregular property using a metamaterial with VO_2. Additionally, the metamaterial performance as a fundamental element of an intelligent windows and that of pigments is also estimated, accounting for the ambient temperatures in Okayama City, the location of the current study, in Japan.

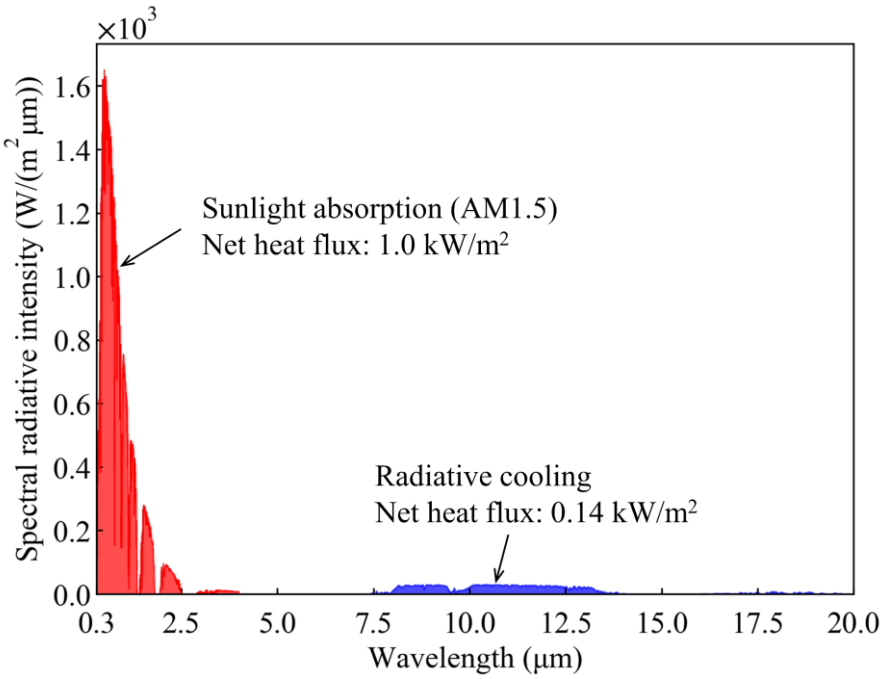

Fig. 1 Comparison of spectral radiative intensity of sunlight and radiative cooling. The red portion of the figure corresponds to solar spectrum known as AM1.5 [1]. The blue portion corresponds to radiative cooling of a blackbody at 300 K through the atmospheric window [25].

2. Theoretical model

Fig. 2 shows a schematic diagram of the multilayered film proposed in the current study. VO_2, silicon dioxide (SiO_2), and VO_2 layers with respective thicknesses of t_1, t_2, and h are deposited on a reflection layer made of gold. Moreover, a slit at the top VO_2 layer with a period of Λ forms a periodic strip structure of width, w. At high temperatures, SiO_2, acting as an insulator, is sandwiched between two metallic VO_2 (m-VO_2) layers. This configuration resembles metal-insulator-metal (MIM) and metal-semiconductor-metal multilayer structures, which significantly absorb or emit thermal radiation of particular wavelengths by resonating the electromagnetic field around them [29–33]. Moreover, SiO_2 has a potential to excite a surface phonon (SPh) in the mid-infrared wavelength range [34] and radiate within a limited bandwidth. Therefore, it is predicted that these phenomena will contribute to enhancing radiative cooling at high temperatures. Alternatively, at low temperatures, VO_2 exists as an insulator (i-VO_2). In this study, the electromagnetic field around the multilayer was numerically calculated to evaluate its absorptivity. Simulations were performed using a two-dimensional finite-difference time-domain (2D-FDTD) method [35,36], employing an open-source software package [37]. In the FDTD method, Maxwell's equations for an electromagnetic field [38], are numerically solved.

$$\nabla \times \mathbf{E}(\mathbf{r},t) = -\frac{\partial \mathbf{B}(\mathbf{r},t)}{\partial t} \tag{1}$$

$$\nabla \times \mathbf{H}(\mathbf{r},t) = \frac{\partial \mathbf{D}(\mathbf{r},t)}{\partial t} + \mathbf{J}(\mathbf{r},t) \tag{2}$$

$$\nabla \cdot \mathbf{D}(\mathbf{r},t) = \rho(\mathbf{r},t) \tag{3}$$

$$\nabla \cdot \mathbf{B}(\mathbf{r}, t) = 0 \tag{4}$$

In the current simulation, the complex permittivities of each material were fitted using several types of dielectric functions. That of gold [39] was fitted to the monopole Drude model as follows:

$$\begin{aligned} \varepsilon_{\mathrm{Au}}(\omega) &= \varepsilon'_{\mathrm{Au}}(\omega) + i\varepsilon''_{\mathrm{Au}}(\omega) \\ &= \varepsilon_\infty - \frac{\omega_\mathrm{p}^2}{\omega(\omega + i\Gamma_\mathrm{p})}, \end{aligned} \tag{5}$$

where, ε_∞ is the relative background permittivity, ω_p is plasma angular frequency, and Γ_p is the relaxation rate of a free electron. That of m-VO_2 [12] was fitted to the Drude–Lorentz model as:

$$\begin{aligned} \varepsilon_{\text{m-VO}_2}(\omega) &= \varepsilon'_{\text{m-VO}_2}(\omega) + i\varepsilon''_{\text{m-VO}_2}(\omega) \\ &= \varepsilon_\infty - \frac{\omega_\mathrm{p}^2}{\omega(\omega + i\Gamma_\mathrm{p})} + \frac{f_{\mathrm{l}1}\omega_{\mathrm{l}1}^2}{\omega_{\mathrm{l}1}^2 - \omega^2 - i\Gamma_{\mathrm{l}1}\omega}, \end{aligned} \tag{6}$$

where, $f_{\mathrm{l}i}$ (i = 1, 2, 3) is the strength of the Lorentz oscillator, $\omega_{\mathrm{l}i}$ (i = 1, 2, 3) is the center angular frequency, and $\Gamma_{\mathrm{l}i}$ (i = 1, 2, 3) is a damping factor. Those of i-VO_2 [12] and SiO_2 [39] were fitted to the dipole or tripole Lorentz models, which are summations of two and three Lorentz oscillators as follows:

$$\begin{aligned} \varepsilon_{\text{i-VO}_2}(\omega) &= \varepsilon'_{\text{i-VO}_2}(\omega) + i\varepsilon''_{\text{i-VO}_2}(\omega) \\ &= \varepsilon_\infty + \frac{f_{\mathrm{l}1}\omega_{\mathrm{l}1}^2}{\omega_{\mathrm{l}1}^2 - \omega^2 - i\Gamma_{\mathrm{l}1}\omega} + \frac{f_{\mathrm{l}2}\omega_{\mathrm{l}2}^2}{\omega_{\mathrm{l}2}^2 - \omega^2 - i\Gamma_{\mathrm{l}2}\omega}, \end{aligned} \tag{7}$$

$$\begin{aligned} \varepsilon_{\mathrm{SiO}_2}(\omega) &= \varepsilon'_{\mathrm{SiO}_2}(\omega) + i\varepsilon''_{\mathrm{SiO}_2}(\omega) \\ &= \varepsilon_\infty + \frac{f_{\mathrm{l}1}\omega_{\mathrm{l}1}^2}{\omega_{\mathrm{l}1}^2 - \omega^2 - i\Gamma_{\mathrm{l}1}\omega} + \frac{f_{\mathrm{l}2}\omega_{\mathrm{l}2}^2}{\omega_{\mathrm{l}2}^2 - \omega^2 - i\Gamma_{\mathrm{l}2}\omega} + \frac{f_{\mathrm{l}3}\omega_{\mathrm{l}3}^2}{\omega_{\mathrm{l}3}^2 - \omega^2 - i\Gamma_{\mathrm{l}3}\omega}. \end{aligned} \tag{8}$$

It is known that i-VO_2 shows phonon absorption bands at wavelengths longer than 17 μm

(< 0.07 eV) [40]. In this study, the effect of phonon band around 17 μm was regarded to be small due to a reason mentioned later. Each parameter in the Drude and Lorentz oscillators is summarized in Table 1.

The numerical simulations were conducted adopting the following assumptions. The complex permittivity of m- or i-VO_2 was appropriately applied for the VO_2 layer to evaluate the absorptivity of the multilayer at high and low temperatures. Ordinarily, the phase transition temperature of VO_2 including the reference [12] is 341 K, which is too high for room temperature control. Technically, the transition temperature can possibly be reduced to 300 K by controlling epitaxial stress in the growth process [9], sputtering deposition [41], and tungsten doping [6]. However, the permittivities of the VO_2 with these techniques are not perfectly same as the original one due to differences of the crystallinity. Specifically, the real permittivity of m-VO_2 should be negative over the visible to mid-infrared range to utilize SPh for absorptivity control. Moreover, the permittivity has a thermal hysteresis loop around the phase transition temperature, and the hysteresis width needs to be reduced enough to achieve good switching property [9,42–44]. Although it is possible to grow VO_2 with preferable permittivity and hysteresis width according to the study in solid physics [9], the permittivity of VO_2 with low transition temperature in a wide wavelength range has not been reported in detail. The objective of the current study is only to reveal the feasibility of the multilayered film using VO_2 as a metamaterial. Therefore, it was assumed that the transition temperature was reduced to 300 K, i.e., room temperature, while retaining the preferable permittivities of m- and i-VO_2 before transition temperature reduction. Simultaneously, the assumption

for the transition temperature enabled to omit the phonon band of i-VO_2 at 17 μm because the phonon absorption becomes less obvious with decreasing temperature difference between the i-VO_2 and transition temperature [45]. Moreover, the hysteresis width was assumed to be negligibly small.

In the simulation, a planar E_x-polarized wave was used to perpendicularly irradiate the multilayer to obtain a spectral absorptivity in the normal direction. The computational area was divided into square mesh with the size of 5 nm × 5 nm. For boundary conditions of the computational area, a perfectly matched layer (PML) was applied to the top and bottom boundaries to eliminate reflections, while a periodic condition was applied to the side boundaries to express an infinite multilayer surface in the *x*-direction. All simulations in this study were conducted using a workstation with an AMD Ryzen 9 3900X processor and 32 GB RAM.

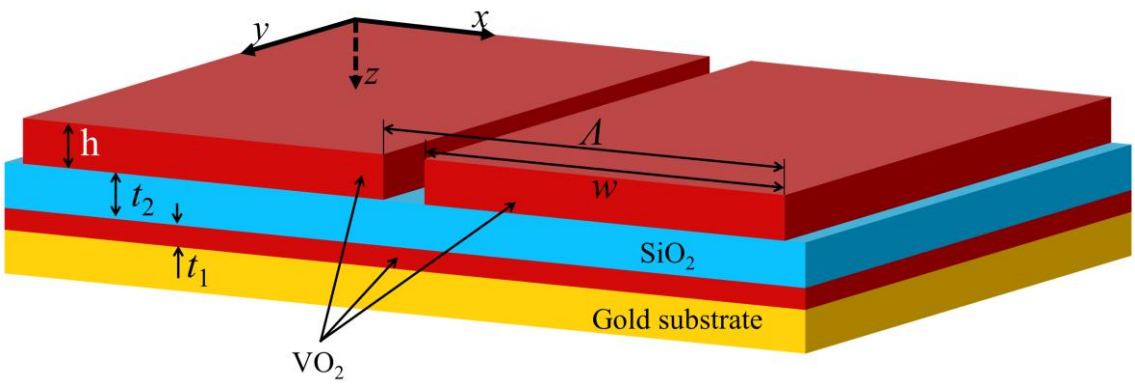

Fig. 2 Schematic diagram of the multilayered film consisting of VO_2.

Table 1 Fitting parameters of the dielectric functions.

Parameters	Gold	m-VO_2	i-VO_2	SiO_2
ε_∞ (-)	3.9703	7.15	5.95	2.38
ω_p (rad/s)	1.2118×10^{16}	9.4×10^{15}	—	—
Γ_p (rad/s)	1.2346×10^{14}	1.55×10^{15}	—	—
f_{l1} (-)	—	2.73	4.5	0.68
ω_{l1} (rad/s)	—	5.58×10^{15}	1.85×10^{16}	2.021×10^{14}
Γ_{l1} (rad/s)	—	1.84×10^{16}	1.55×10^{17}	1.6×10^{12}
f_{l2} (-)	—	—	3.19	0.1
ω_{l2} (rad/s)	—	—	9.8×10^{15}	1.502×10^{14}
Γ_{l2} (rad/s)	—	—	4.6×10^{16}	1.18×10^{12}
f_{l3} (-)	—	—	—	1
ω_{l3} (rad/s)	—	—	—	8.6×10^{13}
Γ_{l3} (rad/s)	—	—	—	6×10^{12}

3. Simulation result and discussion

Fig. 3 shows the spectral absorptivity of the representative geometry with Λ = 2.0 μm, w = 1.8 μm, t_1 = 100 nm, and t_2 = h = 200 nm. For the high temperature condition, the absorptivity diminished to less than 0.5 at the near-infrared range because m-VO_2 has a negative value of permittivity and a reflective property. Therefore, the multilayered film could reflect sunlight to an extent. However, at wavelengths shorter than 0.6 μm, the multilayer absorbed about 80% of the sunlight. Since the permittivity of m-VO_2 is positive in the visible range, the sunlight penetrated into the multilayer with little reflection and was attenuated during a multi-reflection inside the film.

In the mid- and far-infrared range, which involved radiative cooling, there were three distinct peaks at wavelengths of 7.77, 11.74, and 13.21 μm. Blackbody radiation at 300-320 K has a maximum spectral intensity at approximately 9.5 μm. Thus, the three absorptivity peaks easily promoted radiative cooling. A distribution of the *y*-directional magnetic field surrounding the multilayered film is depicted in Fig. 4 to clarify the mechanism of strong emissions at the wavelengths of these three distinct peaks. The incident wave perpendicularly irradiated the surface of multilayered film at a wavelength of 7.77 μm corresponding to the peak wavelength at the shortest side. This peak was chosen because it was the largest of the three distinct peaks. In Fig. 4, the *y*-directional magnetic field was strong inside the SiO_2 layer between which two m-VO_2 layers were sandwiched. The intensity of the magnetic field was more than twice that of the incident wave. Usually, such a strong magnetic field can be described by magnetic response in an

equivalent electrical circuit [29,31,46]. The electrical circuit model is convenient to describe the absorption of radiation by thin-multilayer simply. However, since the carrier relaxation rate of m-VO_2, Γ_p, was higher than the angular frequency of the peak, 2.4 × 10^{14} rad/s, free electrons in the m-VO_2 may not oscillate collectively to form equivalent capacitors and inductors in the circuit model. Moreover, the circuit model indicates wavelengths that are also close to the phonon band of SiO_2. Wang et al. reported an optical phonon has a possibility to mediate a strong LC circuit resonance [47]. However, the circuit model slightly deviated from the simulation result depending on the geometric parameter.

Since the numerical simulation only solves the development of the electromagnetic field, the absorption mechanism essentially could be described as the interaction between the geometry of multilayered film and the surface electromagnetic wave. Instead of the circuit model that expresses the peak wavelength with an analogy, we discuss the state of electromagnetic waves. Generally, an incident wave with a wavelength of several microns cannot enter a 200 nm thick SiO_2 layer sandwiched between two metallic layers because of the diffraction limit. However, an electromagnetic wave with a limited angular frequency and wavenumber can be diffracted at the bottom corner of the strip and exist in the SiO_2 layer as a surface wave that is maintained by the polarized electric charge on metallic surfaces. Here, the local density of electromagnetic states (LDOS) at the VO_2–SiO_2–VO_2 semi-infinite plane layers for a transverse magnetic (TM) wave is expressed for propagating and evanescent components as follows [48]:

$$f_{\mathrm{TM},02}^{\mathrm{prop}}(\omega)=\frac{1}{4\pi^2}\int_0^{\omega/c_0}\frac{(1-\left|r_{10}^{\mathrm{TM}}\right|^2)(1-\left|r_{12}^{\mathrm{TM}}\right|^2)}{\left|1-r_{10}^{\mathrm{TM}}r_{12}^{\mathrm{TM}}e^{2ik_{z1}'t_2}\right|^2}k_x dk_x\,, \tag{9}$$

$$f_{\mathrm{TM},02}^{\mathrm{evan}}(\omega)=\frac{1}{\pi^2}\int_{\omega/c_0}^{\infty}\frac{\mathrm{Im}(r_{10}^{\mathrm{TM}})\,\mathrm{Im}(r_{12}^{\mathrm{TM}})}{\left|1-r_{10}^{\mathrm{TM}}r_{12}^{\mathrm{TM}}e^{2ik_{z1}''t_2}\right|^2}e^{-2k_{z1}''t_2}k_x dk_x\,, \tag{10}$$

where, c_0 is the speed of light in a vacuum, r_{ij} is the Fresnel reflection coefficient between two layers, i and j. The bottom VO_2 layer, SiO_2 layer, and strip layer respectively correspond to layers 0, 1, and 2. Ideally, the layer 0 and 2 need to be sufficiently thick to avoid penetration of electric field. Fig. 5(a) shows the magnitude of the LDOS as functions of the angular frequency of an incident ray and the x-directional wavenumber of the surface wave, k_x. The LDOS had a local maximum at a point with an angular frequency greater than 2.4×10^{14} rad/s and a larger wavenumber than the light line in SiO_2. The local maximum corresponded to the dispersion relation of the surface plasmon (SP), which is the polarized electron on two metallic surfaces sandwiching the insulating layer [49]. Similarly, two series of local maxima and dispersion relations were observed at an angular frequency less than 2.0×10^{14} rad/s. Due to the Lorentzian pole of SiO_2 originating from the SPh oscillation [34], these dispersion relations were separate from that of the SP. Therefore, the dispersion relations were simultaneously affected by the SP and SPh. Here, there was a photonic bandgap with no dispersion relation from 2.0 to 2.3×10^{14} rad/s. Thus, a small incident wave was permitted to enter the trilayer. Its absorptivity was suppressed to a level that was less than 0.3 at wavelengths from 8.0 to 9.0 μm in a vacuum. Although there were dispersion relations at other angular frequencies, several incident rays were still reflected. The wavenumbers of the SP and SPh at the

interface between m-VO_2 and SiO_2 were restricted depending on the strip width, w, due to the finite width of the strip layer. After an incident ray was diffracted at the corner of the strip and converted into a surface wave, only the surface wave whose angular frequency and wavenumber were superposed with the dispersion relation of SP and SPh was absorbed by the multilayered film. The sign of the magnetic field was the same from the left to right sides of the strip, but became zero at the top side of the strip as shown in Fig. 4. This magnetic field possibly corresponded to a half period of the surface wave. Therefore, the wavelength of the surface wave was approximated as double the strip width, and the wavenumber of the surface wave, k_x, corresponded to π/w.

Fig. 5(b) shows the spectral absorptivity of the multilayered film with various strip widths, w. The peak wavelengths estimated by the dispersion relation and the wavenumber, k_x, are depicted by the blue and green dashed lines in this figure. As a reference, the estimated peak wavelength derived using the LC circuit model proposed by Lee et al. was depicted by dashed black lines in Fig. 5(b) [29]. For w = 1.8 μm, the three peaks shown in Fig. 3 were observed. These wavelengths at the peaks decreased with the strip width, w. Here, the wavelengths, which are denoted by each dispersion relation and LC circuit model, also decreased according to the same trend because the larger wavenumber of the surface wave was correlated with the incident ray having a higher angular frequency. The LC circuit model could not express the series of peaks at 12.64 μm, and the model was unsuitable for this geometry to describe the peak without modifications. Moreover, the peak wavelengths denoted by the mixed dispersion relation of the SP and SPh were superposed in the simulation results, especially for the narrow

strip condition. However, there was a discrepancy of several microns between the wavelength denoted by the dispersion relation of the SP and the simulation. The angular frequency of the dispersion relation in the practical geometry was possibly lower than that of the idealized VO_2–SiO_2–VO_2 semi-infinite plane layers. Generally, the dispersion relation of the SP in the multilayer becomes more complicated with increasing numbers of metal and insulating layers [49]. Here, an electromagnetic wave can penetrate even several nanometers into a metal surface. The penetration depth of an electromagnetic wave is $\delta = c_0/2\omega\kappa$, where the intensity of the wave attenuates at the rate of e^{-1} for m-VO_2, is about 50 nm. Here, $\kappa = \sqrt{\left(-\varepsilon' + \sqrt{\varepsilon'^2 + \varepsilon''^2}\right)/2}$ is an extinction coefficient. Since the thickness of the bottom m-VO_2 layer was 100 nm, not thick enough to eliminate the electromagnetic wave, the substrate gold layer affected the dispersion relation of the SP. The SP and SPh affected the absorptivity at the peak wavelength as well. For w = 0.5 μm, two peaks were observed at 9.43, and 12.64 μm, and their absorptivities were comparatively low. Since the strip only covered 25% of the SiO_2–vacuum interface, the incident ray could not strongly excite the SPh or SP to become absorbed. Conversely, the absorptivities at the peaks and the full width at half maximum (FWHM) became larger with increasing strip width. It is clear that the wide strip had a role to enhance absorptivity in the infrared range by exciting the SP and SPh inside SiO_2 layer at high temperatures.

Fig. 3 also shows spectral absorptivity for the low temperature condition when VO_2 shows insulating characteristics. The overall absorptivity for an infrared ray was lower than at high temperatures. Although two significant peaks were observed at a

wavelength of 8 μm, they only slightly contributed to promoting radiative cooling due to their small FWHM. On the contrary, the overall absorptivity for the visible ray reached about 0.8 due to the overlap of several peaks with large FWHMs. The high absorptivity in the visible range is useful to efficiently harvest sunlight energy.

The current geometry presents three transparent films on a reflection substrate. Their absorptivities are often determined by the thickness of each layer in similar geometries [50]. Fig. 6(a) shows the spectral absorptivity with various thicknesses of the bottom VO_2 layer, t_1, from 0 to 1000 nm. The strip width, w, was fixed at 1.8 μm. The peaks at 8.77 and 12.5 μm were not affected by the thickness, t_1. Due to the Lorentz oscillators' center frequencies, ω_{l1} and ω_{l2} shown in Table 1, SiO_2 has negative permittivity values at wavelengths from 8.1 to 9.3 μm and 12.4 to 12.53 μm. In contrast, vacuum and i-VO_2 have positive values at these wavelengths. The absorptivity of a multilayer sometimes has a local maximum originating from the excitation of the SPhP at the interface between two non-magnetic materials when their permittivities are of opposite signs [34]. Here, the SPhP has the following dispersion relation [51]:

$$k_{\mathrm{SPhP}} = (\omega/c_0)\sqrt{\varepsilon_1\varepsilon_2/(\varepsilon_1+\varepsilon_2)}, \tag{11}$$

where, k_{SPhP} is the wavenumber of the SPhP in the x-direction and ε_i is the permittivity of the medium, i. The SPhP can be excited by a TM polarized propagation wave, which both satisfy the SPhP's dispersion relation and the following Bloch condition:

$$k_{x,n} = \omega/c_0 + 2\pi n/\Lambda, \tag{12}$$

where, n is the order of diffraction in the x-direction. The green and blue lines in Fig. 6(a) show the wavelength of the incident rays, which respectively excite the SPhP at the SiO_2–vacuum and SiO_2–i-VO_2 interfaces. The two modes of the SPhP were excited at the almost same wavelength, 12.3 and 12.6 μm. Since the FWHMs of the two modes were larger than the difference of the resonant wavelengths, there was a single absorptivity peak at 12.5 μm. The theoretical SPhP wavelength was also superposed on two absorptivity peaks around 9.0 μm for VO_2 layers thicker than 500 nm. Fig. 7(a) shows an image of the y-directional magnetic field around the multilayered film for t_1 = 600 nm. The wavelength of the incident ray was 8.64 μm, which corresponds to that of the SPhP between SiO_2 and the vacuum. Usually, the SPhP cannot be excited by a normal incident wave because the wavenumber in the x-direction is zero. Since a portion of the incident wave was diffracted at the top and bottom corners of the strip, the wave could satisfy the dispersion relation of the SPhP. Therefore, a strong magnetic field was selectively observed at the SiO_2–vacuum interface, while the absolute intensity was comparatively weak at other interfaces. Fig. 7(b) also shows a distribution of the magnetic field at 9.16 μm corresponding to the SPhP wavelength between SiO_2 and i-VO_2. The magnetic field at the bottom surface of the i-VO_2 strip was enhanced along the SiO_2–i-VO_2 interface. Simultaneously, the magnetic field at the interface below the slit between two strips was also enhanced with an opposite sign to other interfaces. It is considered that the SPhP was partially observed because the diffraction of the incident wave at the bottom corners of the strip restricted possible wavenumbers in the SiO_2 layer.

However, the two absorptivity peaks at around 9.0 μm slightly deviated from the SPhP modes for t_1 = 100 nm. The peak with a shorter wavelength was possibly a mixed SPhP mode because it split into two SPhP modes with increasing thickness of i-VO_2, t_1. Conversely, the peak wavelength of the second peak increased proportionally to the i-VO_2 thickness and completely deviated from the SPhP wavelength. Moreover, this peak was determined analytically using Fresnel's equation for the multilayer assuming a top layer with no slit between the two strips. It was because the slit width was relatively small. Thus, optical interference in the multilayer affected the absorptivity, including the SPhP modes [38]. A proportional increase of peak wavelength was also observed in the visible and near-infrared ranges. Fig. 6(b) shows an expanded contour of absorptivity of the indicated area in Fig. 6(a). Proportional increases of the peaks were clear, especially at wavelengths greater than 2.0 μm. Furthermore, three peaks in this wavelength range corresponded well to the analytical results depicted by the dashed lines because diffraction at the slit was negligible. Here, peak wavelengths less than 2.0 μm were nearly independent of the thickness, t_1, and kept its wavelength constant when t_1 was larger than 100 nm. The Fresnel's equation indicated that these peaks originated from optical interference only at the top i-VO_2 and SiO_2 layers. The thickness of the bottom i-VO_2 only affected the optical interference when it was smaller than 50 nm. In summary, most of the peak wavelengths at low temperature conditions were consistent with optical interference, except the SPhP modes at resonant wavelengths.

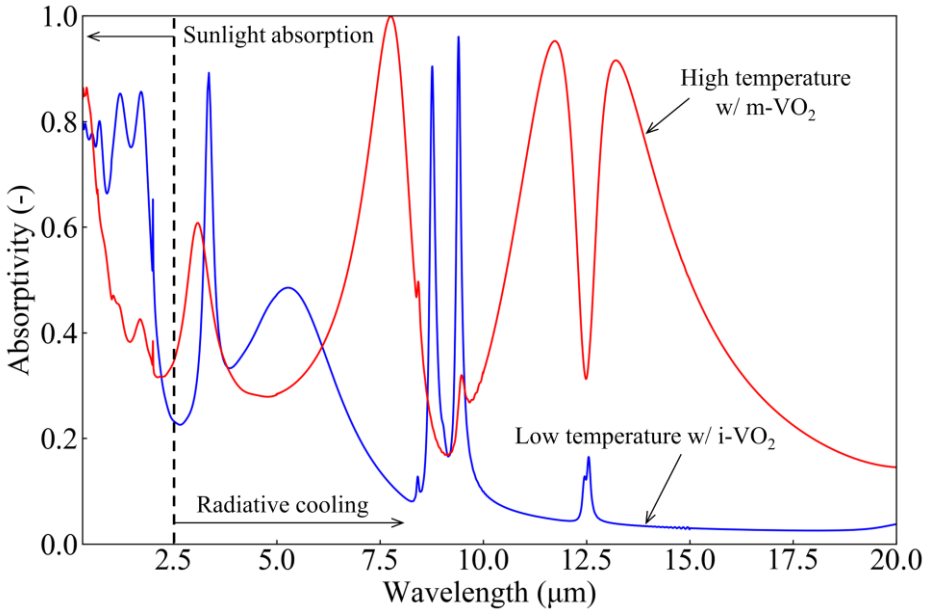

Fig. 3 Spectral absorptivity of the thin multilayer consiting of VO_2. The red and blue lines respectively show the absorptivity at high and low temperatures.

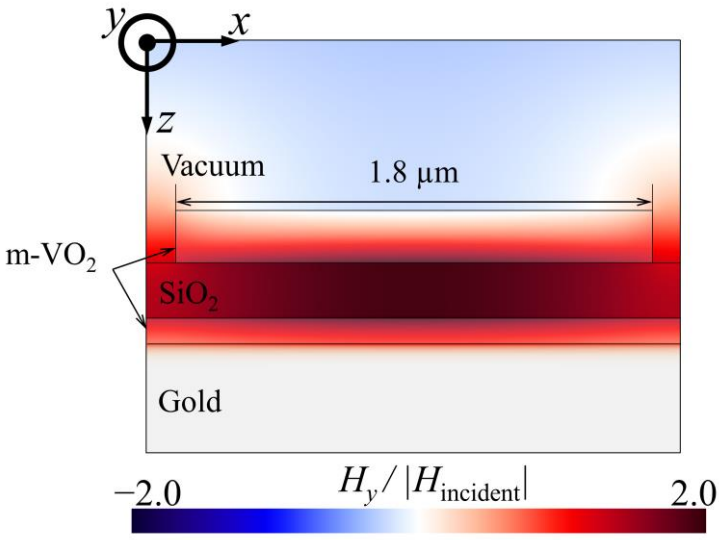

Fig. 4 The distribution of the *y*-directional magnetic field around the multilayed film whose strip width is 1.8 μm. The wavelength of the incident wave is 7.77 μm.

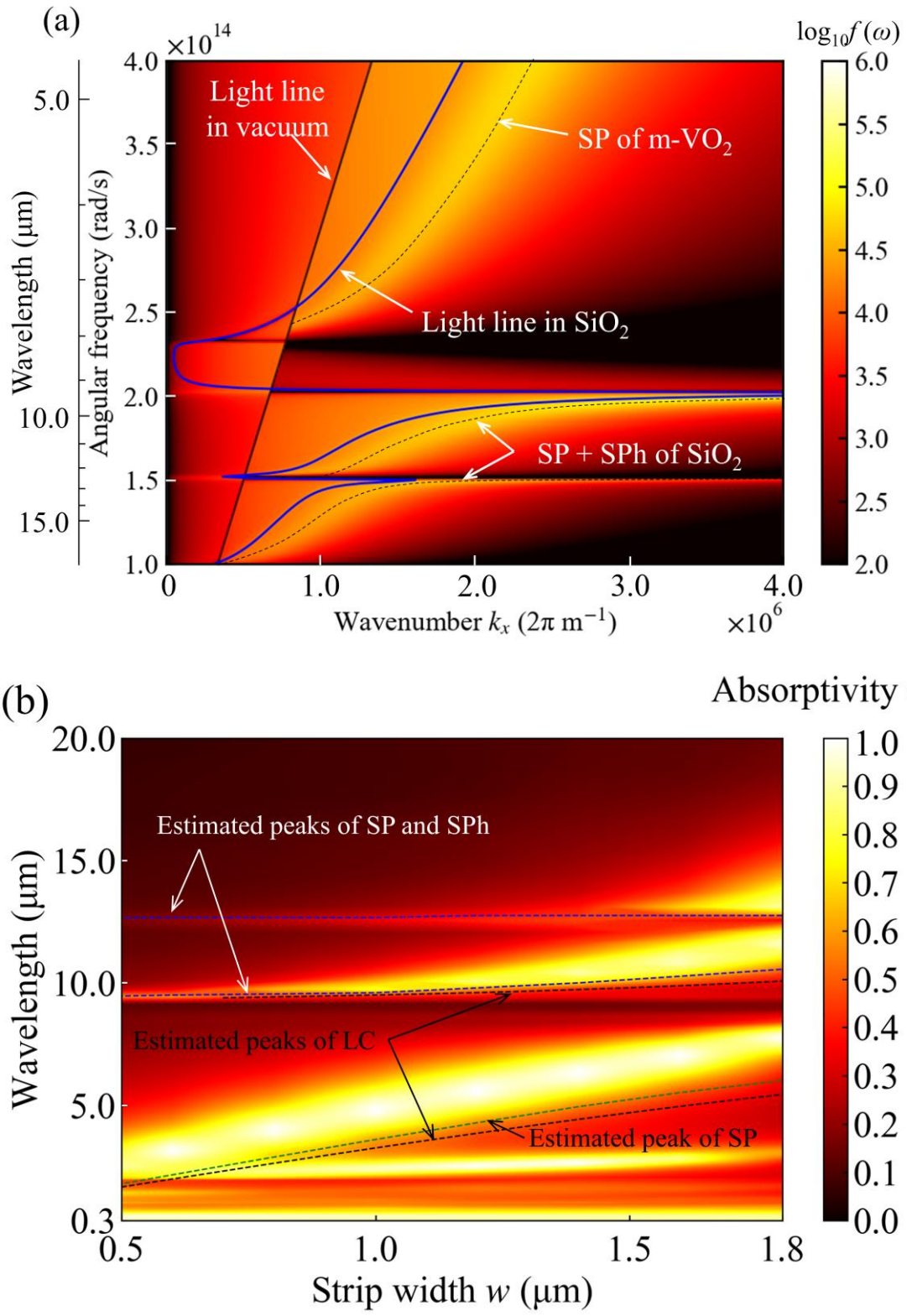

Fig. 5 (a) Logarithmic intensity of local density of states, $f(\omega)$, for the surface wave inside the SiO_2 channel sandwiched between two smooth m-VO_2 planes. The thickness of the

SiO_2 layer is 200 nm. The local maxima of $f(\omega)$ are depicted by dashed lines. (b) Spectral absorptivity of the multilayered film with various strip widths, w, is dipicted by contours. The pitch of the periodic structure, Λ, is set to 2.0 μm. The blue dashed lines show the wavelength where the mixed dispersion relation of the SP and SPh corresponds to the wavenumber of the surface wave, k_x. The green dashed line shows the dispersion relation of the SP.

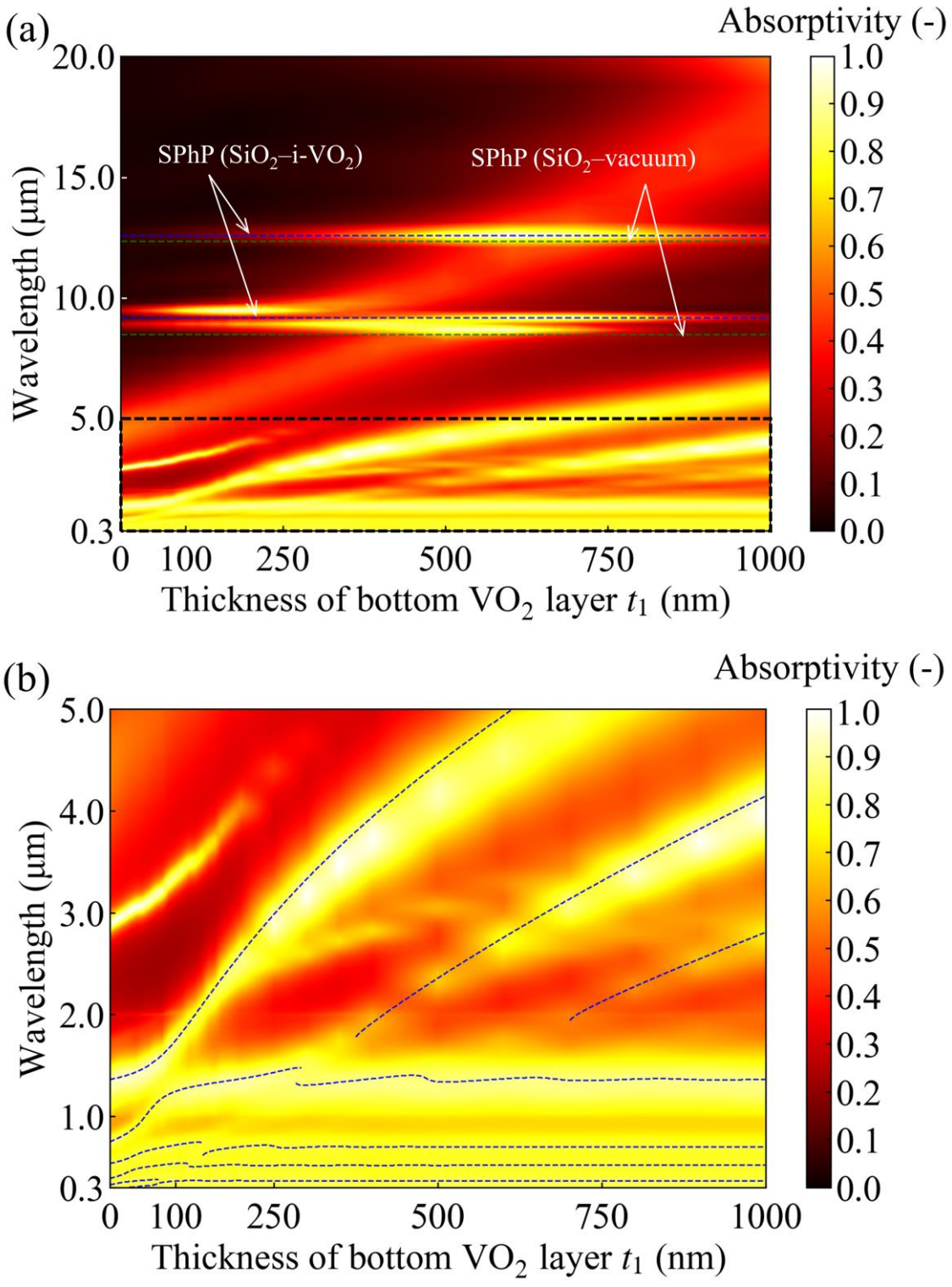

Fig. 6 Spectral absorptivity of the multilayered film with various thicknesses of the bottom i-VO_2 layer, t_1. The region enclosed by black dashed lines in (a) is expanded in

(b). The blue dashed lines in (b) show peak wavelengths for the multilayer with no slit on the top layer, analytically obtained from Fresnel's equation.

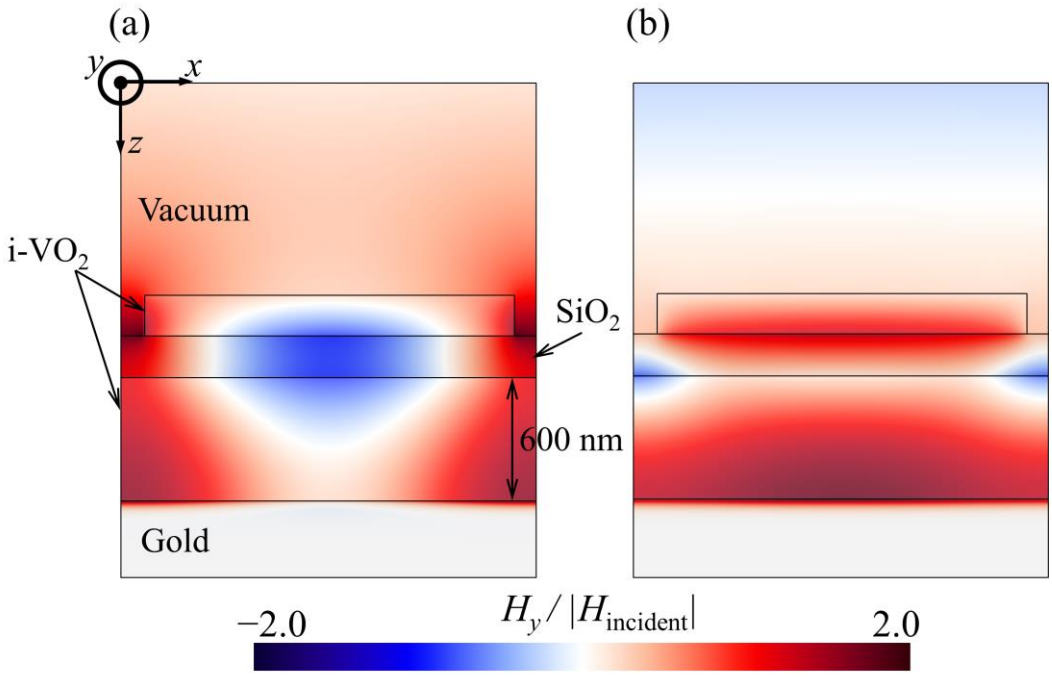

Fig. 7 The distributions of the *y*-directional magnetic field around the multilayered film. The thickness of the bottom i-VO_2 layer is 600 nm. The wavelengths of the incident wave are (a) 8.64 and (b) 9.16 μm.

4. Performance assessment

To evaluate the performance of the multilayered film as a fundamental element of the intelligent pigment, the radiative heat flux between the space and film was simply calculated. Note that this assessment was based on the permittivity of m- and i-VO_2, which were used for numerical simulation, while the fluctuation of the properties originating from the manufacturing process was not taken into account. When the film at temperature, T, absorbs sunlight and radiates thermally, the spectral intensity of absorption, $E_{\mathrm{in},\lambda}$, and emission, $E_{\mathrm{out},\lambda}$, are derived as follows:

$$E_{\mathrm{in},\lambda} = \alpha_\lambda E_{\mathrm{AM1.5},\lambda}\,, \tag{13}$$

$$E_{\mathrm{out},\lambda}(T) = \alpha_\lambda T_{\mathrm{Atm}} E_{\mathrm{BB},\lambda}(T)\,, \tag{14}$$

where, α_λ is the spectral absorptivity of the multilayered film, T_{Atm} is the atmospheric transmittance, $E_{\mathrm{AM1.5},\lambda}$ is the spectral intensity of AM1.5, and $E_{\mathrm{BB},\lambda}(T)$ is the Planck distribution at temperature, T. In this study, absorption and emission only in the normal direction were considered for convenience. Moreover, the total absorbed and emitted energies, E_{in} and E_{out}, are respectively derived from the integrals of $E_{\mathrm{in},\lambda}$ and $E_{\mathrm{out},\lambda}$ as follows:

$$E_{\mathrm{in}} = \int_0^\infty E_{\mathrm{in},\lambda} d\lambda\,, \tag{15}$$

$$E_{\mathrm{out}}(T) = \int_0^\infty E_{\mathrm{out},\lambda}(T) d\lambda\,. \tag{16}$$

In this study, these integrals were calculated over the range from 0.3 to 20 μm, where almost 100% of sunlight energy and radiative energy from the ground are included considering the atmospheric transmittance [25]. Fig. 8(a) shows the spectral intensity of

the sunlight absorbed by the multilayered film with Λ = 2.0 μm, w = 1.8 μm, t_1 = 100 nm, and t_2 = h = 200 nm at high and low temperatures. The spectral intensity from 0.6 to 1.8 μm at high temperatures is slightly suppressed compared with the lower temperature case. As a result, the absorbed heat flux at a high temperature becomes 626 W/m^2, smaller than that at low temperature, 747 W/m^2. However, the multilayered film at high temperature still absorbs 62% of sunlight energy due to the transparency of m-VO_2 at a wavelengths shorter than 0.5 μm. Fig. 8(b) shows the spectral intensity of the thermal radiation from the multilayered film at high and low temperatures. The temperatures of the multilayer were set at 303 or 278 K, which are respectively the average temperatures of Okayama City in August 2020 and January 2021 [52]. The heat flux of thermal radiation at 303 K was 79.8 W/m^2, which was seven times larger than that at 278 K, 11.5 W/m^2. The Planck distributions at room temperature had their maximum values at around 10 μm. Here, the large FWHMs of absorptivity peaks at 303 K covered the wavelength range of the atmospheric window. Thus, radiative cooling was promoted. Conversely, two peaks originating from the SPhP and optical interference at 278 K slightly contributed to radiative cooling due to their extremely narrow FWHMs. The SPhP was usually applied for enhancing radiative cooling [26], however, it conveniently functioned in suppression in the current case. It was clear that the SPh related phenomena were possibly utilized for both enhancing and suppressing radiative cooling with thermochromic materials.

As a summary discussion of absorption and radiative heat flux, we roughly evaluated the performance of a multilayered film as an intelligent pigment for building from the viewpoint of a daily heat balance by subtracting the component of radiative

cooling from the sunlight absorption. Here, the daylight hours in Okayama City are 14.5 hours in summer, but only 10.0 hours in winter [52]. Alternatively, radiative cooling of the ground is passively conducted throughout the day. When the contributions of weather, humidity and sunlight angle to both sunlight absorption and radiative cooling were ignored, the daily average of the radiative heat flux between outer space and the multilayered film, E_{Ave}, was defined as follows:

$$E_{\mathrm{Ave}} = \frac{t_{\mathrm{Daylight}} E_{\mathrm{in}} - t_{\mathrm{Day}} E_{\mathrm{out}}}{t_{\mathrm{Day}}}, \tag{17}$$

where, t_{Daylight} (hours) is the daylight time when the multilayered film can absorb the sunlight, and t_{Day} = 24 h is the hours of one day, neglecting leap years and seconds. The daily averages of the heat flux were 296 W/m^2 and 299 W/m^2 at high and low temperature conditions, respectively. Here, those of ordinary building materials became 364 and 254 W/m^2 in summer and winter, assuming an emissivity of 0.8 over the whole wavelength range [53–55]. The multilayered film had the potential to maintain a heat flux throughout the year due to the phase transition of VO_2. Thus, it can reduce the heat flux in summer while increasing it in winter compared with ordinary building materials.

Finally, we discuss the relationship between the daily average of heat flux and multilayered film geometry. Fig. 9(a) shows the radiative energy absorbed by the multilayered film with various strip widths, *w*, at 303 K. The multilayered film absorbed less radiative energy with increasing strip width. This net energy absorption can be reduced by strongly promoting radiative cooling. In the high temperature case, as shown in Fig. 6, the intensity and FWHW of the SPh modes also became greater with increasing

strip width. However, the slit width between the two strips cannot be ignored from the perspective of manufacturing. The thickness of the top VO_2 strip needs to be greater than 200 nm to excite the SPh modes at the SiO_2 layer. The aspect ratio of the slit, $h/(\Lambda - w)$, should be less than 1.0 at a minimum. Thus, the strip width, w, of 1.8 μm is considered a provisional optimum value. Fig. 9(b) shows the daily average of heat flux at 278 K with various bottom i-VO_2 layer thicknesses. The heat flux increased with thickness, t_1, at values greater than 600 nm. However, this thickness is infeasible from the perspective material costs and manufacturing speed. When the thickness of the bottom i-VO_2 is thinner than 600 nm, the heat flux increases with decreasing thickness, t_1. This is because the peak wavelengths of absorptivity become shorter with decreasing thickness, t_1, as shown in Fig. 6(b), contributing to the effective absorption of sunlight energy. Alternatively, the bottom layer of VO_2 needs to be thick enough to excite the SPh and promote radiative cooling at high temperatures. Moreover, the heat flux at $t_1 = 0$ is smaller than that at $t_1 = 100$ nm due to fewer absorptivity peaks from the optical interference. As a result, a thickness, t_1, of 100 nm seems to be the best point of compromise in the current geometry and VO_2. In practical manufacturing, the real part of permittivity of i-VO_2 correlating to optical interferences has a slight uncertainty depending on the crystallinity of VO_2; thus, t_1 needs further adjustment to maximize the sunlight absorption.

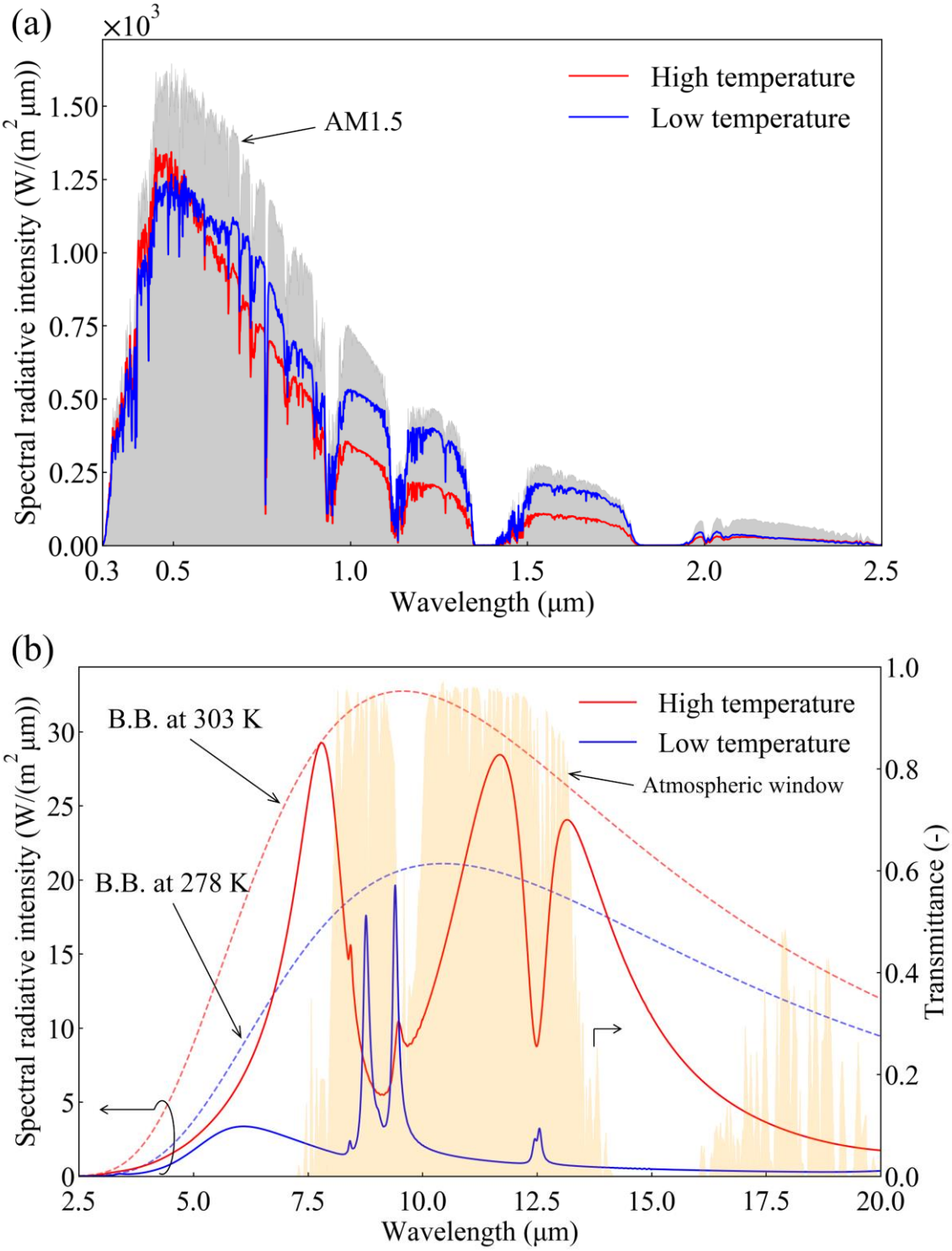

Fig. 8 Spectral radiative intensity of (a) sunlight absorption and (b) radiative cooling. The gray region depicts solar radiation (AM1.5 [1]) and orange area illustrates the transmittance of the atmospheric window [25]. Solid blue and red lines show spectral

radiative intensities at low and high temperatures, respectively. Dashed blue and red lines show Planck distributions at 303 K and 278 K, respectively.

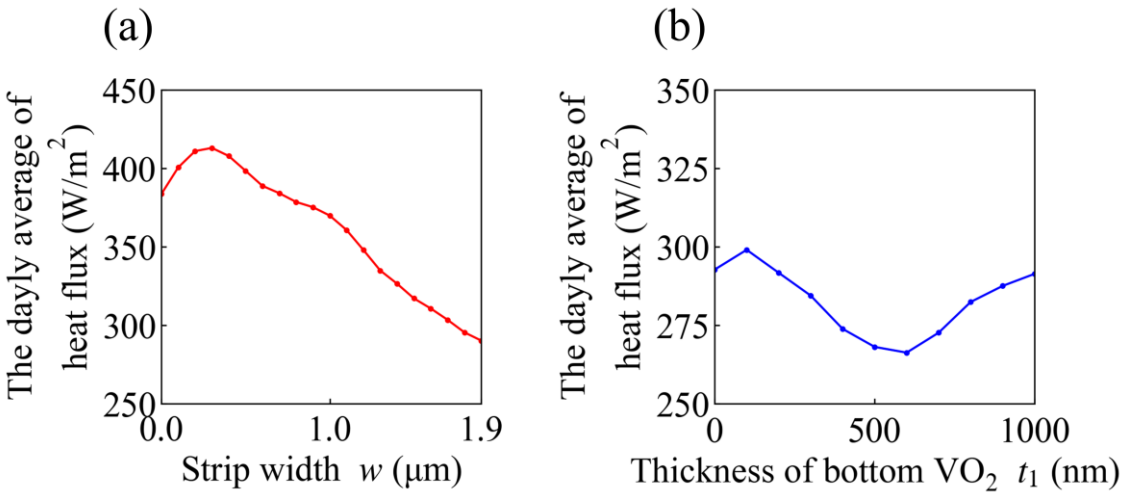

Fig. 9 (a) The relation between daily average of heat flux and strip width, w, at 303 K. (b) The relation between daily average of heat flux and thickness of the bottom VO_2 layer, t_1, at 278 K.

5. Conclusions

We propose a multilayered film consisting of VO_2, SiO_2, and, gold as a metamaterial to control the balance between sunlight absorption and radiative cooling as a function of the ambient temperature. The performance of the metamaterial is numerically estimated through the FDTD simulations. At high temperatures, the absorptivity of the multilayer shows three distinct peaks at mid-infrared wavelengths related to the atmospheric window. The dispersion relation of m-VO_2–SiO_2–m-VO_2 semi-infinite plane layers shows that these peaks originate from the SP and SPh, which are excited at the SiO_2 layer. The VO_2 strip width approximately determined the peak wavelengths and intensities following the dispersion relation. On the contrary, the multilayer had comparatively low absorptivity at visible and near-infrared wavelengths due to the metallic characteristics of VO_2. Thus, the multilayered film exhibited a lower daily average heat flux than would be the case using ordinary building materials in summer. At a low temperature, the absorptivity of the multilayer at the atmospheric window is well suppressed, except for two narrow peaks. The dispersion relation and Fresnel's equation show that these two peaks originate from the SPhP and optical interference at the interface between SiO_2–vacuum and SiO_2–i-VO_2. Since FWHMs of SPhPs were narrow enough, these peaks contribute little to radiative cooling. Conversely, optical interference functions to increase the sunlight absorption in the visible range. Therefore, the multilayer exhibited a larger daily average heat flux than if ordinary building materials were used in winter.

Acknowledgement

This work was supported by the Japan Society for the Promotion of Science (JSPS) KAKENHI Grant in Aide for Research Activity Start-up (Number: 20K22394).

References

1. C. A. Gueymard, Sol. Energy **71**, 325 (2001).
2. A. Synnefa, M. Santamouris, and K. Apostolakis, Sol. Energy **81**, 488 (2007).
3. J. Lv, M. Tang, R. Quan, and Z. Chai, Ceram. Int. **45**, 15768 (2019).
4. G. B. Smith, A. Gentle, P. Swift, A. Earp, and N. Mronga, Sol. Energy Mater. Sol. Cells **79**, 163 (2003).
5. I. P. Parkin and T. D. Manning, J. Chem. Educ. **83**, 393 (2006).
6. N. Wang, S. Magdassi, D. Mandler, and Y. Long, Thin Solid Films **534**, 594 (2013).
7. M. E. A. Warwick and R. Binions, J. Mater. Chem. A **2**, 3275 (2014).
8. R. Zhang, B. Xiang, M. Feng, Y. Xu, L. Xu, and L. Xia, J. Mater. Sci. **55**, 10689 (2020).
9. Y. Muraoka, Y. Ueda, and Z. Hiroi, J. Phys. Chem. Solids **63**, 965 (2002).
10. M. Currie, M. A. Mastro, and V. D. Wheeler, Opt. Mater. Express **7**, 1697 (2017).
11. A. Ueno, J. Kim, and H. Nagano, Int. J. Heat Mass Transf. **166**, 120631 (2021).
12. M. J. Dicken, K. Aydin, I. M. Pryce, L. A. Sweatlock, E. M. Boyd, S. Walavalkar, J. Ma, and H. A. Atwater, Opt. Express **17**, 18330 (2009).
13. S. Wang, K. A. Owusu, L. Mai, Y. Ke, Y. Zhou, P. Hu, S. Magdassi, and Y. Long, Appl. Energy **211**, 200 (2018).
14. Y. Dachuan, X. Niankan, Z. Jingyu, and Z. Xiulin, J. Phys. D. Appl. Phys. **29**, 1051 (1996).
15. Y. Zhang, S. Qiao, L. Sun, Q. W. Shi, W. Huang, L. Li, and Z. Yang, Opt. Express **22**, 11070 (2014).
16. S. Chen, H. Ma, J. Dai, and X. Yi, Appl. Phys. Lett. **90**, (2007).
17. M. A. Kats, R. Blanchard, S. Zhang, P. Genevet, C. Ko, S. Ramanathan, and F. Capasso, Phys. Rev. X **3**, 041004 (2013).
18. H. Kocer, S. Butun, B. Banar, K. Wang, S. Tongay, J. Wu, and K. Aydin, Appl. Phys. Lett. **106**, (2015).
19. K. Sun, C. A. Riedel, A. Urbani, M. Simeoni, S. Mengali, M. Zalkovskij, B. Bilenberg, C. H. de Groot, and O. L. Muskens, ACS Photonics **5**, 2280 (2018).
20. L. Long, S. Taylor, X. Ying, and L. Wang, Mater. Today Energy **13**, 214 (2019).
21. K. Ito, T. Watari, K. Nishikawa, H. Yoshimoto, and H. Iizuka, APL Photonics **3**, (2018).

22. R. L. Voti, M. C. Larciprete, G. Leahu, C. Sibilia, and M. Bertolotti, J. Appl. Phys. **112**, (2012).
23. T. Chang, X. Cao, L. R. Dedon, S. Long, A. Huang, Z. Shao, N. Li, H. Luo, and P. Jin, Nano Energy **44**, 256 (2018).
24. V. G. Golubev, V. Y. Davydov, N. F. Kartenko, D. A. Kurdyukov, A. V. Medvedev, A. B. Pevtsov, A. V. Scherbakov, and E. B. Shadrin, Appl. Phys. Lett. **79**, 2127 (2001).
25. A. Raman, M. A. Anoma, L. Zhu, E. Rephaeli, and S. Fan, Nature **515**, 540 (2014).
26. E. Rephaeli, A. Raman, and S. Fan, Nano Lett. **13**, 1457 (2013).
27. T. Liu and J. Takahara, Opt. Express **25**, A612 (2017).
28. J. Kou, Z. Jurado, Z. Chen, S. Fan, and A. J. Minnich, ACS Photonics **4**, 626 (2017).
29. B. J. Lee, L. Wang, and Z. M. Zhang, Opt. Express **16**, 11328 (2008).
30. R. Feng, J. Qiu, L. Liu, W. Ding, and L. Chen, Opt. Express **22**, A1713 (2014).
31. A. Sakurai, B. Zhao, and Z. M. Zhang, J. Quant. Spectrosc. Radiat. Transf. **149**, 33 (2014).
32. X. Han, K. He, Z. He, and Z. Zhang, Opt. Express **25**, A1072 (2017).
33. K. Isobe, R. Okino, and K. Hanamura, Opt. Express **28**, 40099 (2020).
34. S. Shen, A. Narayanaswamy, and G. Chen, Nano Lett. **9**, 2909 (2009).
35. A. Taflove and S. C. Hagness, *Computational Electrodynamics: The Finite-Difference Time-Domain Method*, 3rd ed. (Artech House on Demand, 2005).
36. A. Taflove, A. Oskooi, and S. G. Johnson, *Advances in FDTD Computational Electrodynamics: Photonics and Nanotechnology* (Artech: Norwood, Massachusetts, 2013).
37. A. F. Oskooi, D. Roundy, M. Ibanescu, P. Bermel, J. D. Joannopoulos, and S. G. Johnson, Comput. Phys. Commun. **181**, 687 (2010).
38. R. Siegel and J. R. Howell, *Thermal Radiation Heat Transfer*, 2nd ed. (Hemisphere Publishing Corporation, New York, 1981).
39. E. D. Palik., *Handbook of Optical Constants of Solids: Volume 1.* (Academic Press, San Diego, California, 1985).
40. P. J. Van Zwol, K. Joulain, P. Ben-Abdallah, and J. Chevrier, Phys. Rev. B - Condens. Matter Mater. Phys. **84**, 1 (2011).
41. H. Hoshino, K. Okimura, I. Yamaguchi, and T. Tsuchiya, Sol. Energy Mater. Sol. Cells **191**, 9 (2019).
42. T. Cesca, C. Scian, E. Petronijevic, G. Leahu, R. Li Voti, G. Cesarini, R. Macaluso,

M. Mosca, C. Sibilia, and G. Mattei, Nanoscale **12**, 851 (2020).
43. G. Cesarini, G. Leahu, R. Li Voti, and C. Sibilia, Infrared Phys. Technol. **93**, 112 (2018).
44. G. Cesarini, G. Leahu, A. Belardini, M. Centini, R. Li Voti, and C. Sibilia, Int. J. Therm. Sci. **146**, 106061 (2019).
45. A. S. Barker, H. W. Verleur, and H. J. Guggenheim, Phys. Rev. Lett. **17**, 1286 (1966).
46. N. Engheta, Science **317**, 1698 (2007).
47. L. Wang and Z. M. Zhang, Opt. Express **19**, A126 (2011).
48. M. Francoeur, M. P. Mengüç, and R. Vaillon, J. Quant. Spectrosc. Radiat. Transf. **110**, 2002 (2009).
49. E. N. Economou, Phys. Rev. **182**, 539 (1969).
50. A. Sakurai, K. Yada, T. Simomura, S. Ju, M. Kashiwagi, H. Okada, T. Nagao, K. Tsuda, and J. Shiomi, ACS Cent. Sci. **5**, 319 (2019).
51. H. Wang and L. Wang, J. Quant. Spectrosc. Radiat. Transf. **158**, 127 (2015).
52. Japan Meteorological Agency, (2021), https://www.data.jma.go.jp/obd/stats/etrn/index.php. Accessed 21 March 2021.
53. Z. J. Ye, C. F. Ma, and S. Y. Huang, J. Therm. Sci. **5**, 128 (1996).
54. N. P. Avdelidis and A. Moropoulou, Energy Build. **35**, 663 (2003).
55. S. Kotthaus, T. E. L. Smith, M. J. Wooster, and C. S. B. Grimmond, ISPRS J. Photogramm. Remote Sens. **94**, 194 (2014).